Nano Energy 86 (2021) 106029

Contents lists available at ScienceDirect

Nano Energy

journal homepage: http://www.elsevier.com/locate/nanoen

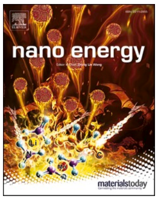

A high-entropy phosphate catalyst for oxygen evolution reaction

Haiyu Qiao [a,1], Xizheng Wang [a,1], Qi Dong [a,1], Hongkui Zheng [b,1], Gang Chen [a], Min Hong [a], Chun-Peng Yang [a], Meiling Wu [a], Kai He [b,*], Liangbing Hu [a,c,**]

[a] Department of Materials Science and Engineering, University of Maryland, College Park, MD 20742, United States
[b] Department of Materials Science and Engineering, Clemson University, Clemson, SC 29634, United States
[c] Center for Materials Innovation, University of Maryland, College Park, MD 20742, United States

ARTICLE INFO

Keywords:
High-entropy phosphate
Catalyst
High-temperature
Aerosol
Oxygen evolution reaction

ABSTRACT

Transition metal phosphates are a class of catalysts that are widely used in biologic reactions, organic synthesis, oxygen evolution, and photocatalysis. While previous studies have shown the catalytic performance can be greatly benefited from incorporating multiple elements, high-entropy polyanionic materials such as high-entropy phosphates (HEPi) have never been reported due to the harsh synthetic requirement of a short high-temperature heating duration. Herein we for the first time report the synthesis of HEPi catalyst (*i.e.*, CoFeNiMnMoPi) in the form of highly uniform spherical particles through a high-temperature fly-through method. Our approach enables (1) uniformly confined metal and phosphorous precursors in one aerosol droplet, (2) *in-situ* oxide-to-phosphate transformation at high temperature, and (3) homogenous mixing of multi-metallic elements in a phosphate structure in milliseconds. As a proof-of-concept, we apply the HEPi catalyst in a model oxygen evolution reaction (OER), where much lower overpotential (270 mV at 10 mA cm^{-2}) and faster kinetics (Tafel slope of 74 mV dec^{-1}) were measured compared to the commercial IrO_x and the high-entropy oxide (HEO) counterpart. This study paves a new way toward synthesizing a library of high-entropy polyanionic compounds for a range of applications in energy and catalysis.

1. Introduction

The fast development in the fields of energy and catalysis has spurred the discoveries of new compounds that keep enriching the materials genome [1–5]. Recently, significant attentions have been paid to the multi-elemental or high-entropy compounds that incorporate multiple metallic elements uniformly distributed in a solid solution [6–10]. Owing to the synergistic effect and high-entropy stabilization, these compounds typically show greatly improved catalytic activity and stability [11–13]. However, the multi-elemental and high-entropy compounds developed so far are limited to monoanionic species such as oxides [14,15], carbides [16], and sulfides [17,18] that are in relatively simple molecular structures. While the combinatorial elemental choices were broadened through implementing the high-entropy concept, there still exists a vast material space to be discovered by extending the synthetic capability to more complex systems such as polyanionic materials [19–22]. In particular, transition metal phosphates are a class of catalysts that have been widely employed in a range of reactions such as biologic transformation (*e.g.*, vanadyl phosphate [23,24]), organic synthesis (*e.g.*, zirconium phosphate [25]), oxygen evolution (*e.g.*, cobalt phosphate, also widely known as CoPi [26–29]) and photocatalysis (*e.g.*, Ag_3PO_4 [30]). The polyanionic nature of these compounds embraces unique electronic states and surface structures that are distinct from the commonly used oxide catalysts or others, which hold good promise for fast kinetics, good selectivity, or both. To synthesize high-entropy phosphate (HEPi, in accordance with literature practice for the abbreviation of inorganic phosphate species), high temperature is needed for the effective decomposition of various precursors, meanwhile a short heating duration is also crucial to avoid elemental segregation or phase separation. However, these requirements are beyond the capability of conventional synthetic methods, thus hindering the potential of HEPi materials to be realized.

Herein, we for the first time report the synthesis of a HEPi catalyst (*i.e.*, CoFeNiMnMoPi) in the form of highly uniform spherical particles.

---

[*] Corresponding author.
[**] Corresponding author at: Department of Materials Science and Engineering, University of Maryland, College Park, MD 20742, United States.
E-mail addresses: kaihe@clemson.edu (K. He), binghu@umd.edu (L. Hu).
[1] These authors contributed equally to this work.

https://doi.org/10.1016/j.nanoen.2021.106029
Received 11 November 2020; Received in revised form 28 February 2021; Accepted 25 March 2021

Our synthetic method features a high-temperature fly-through process using aerosols that confine metal and phosphorous precursors uniformly distributed in individual droplets. During the high-temperature and rapid heating process, an oxide-to-phosphate transformation can be completed *in-situ* to ensure the homogenous elemental mixing in a phosphate phase in milliseconds. We employ the high-temperature fly-through method to synthesize a series of mono-metallic, trimetallic and high-entropy phosphate compounds. To satisfy different requirements for catalytic reactions, the particle size can be well controlled by tuning the synthesis parameters (*e.g.*, concentration of precursors, flow rate, synthetic temperature, *etc.*) in the fly-through process. Meanwhile, the spherical particles can also be made into hollow structures *in-situ* due to the decomposition of tri-n-octylphosphine oxide (TOPO) as the phosphorous sources (Fig. S1). We apply the HEPi particles as electrocatalyst in a model oxygen evolution reaction (OER), where much lower overpotential (270 mV at 10 mA cm^{-2}) and faster kinetics (74 mV dec^{-1}) can be achieved compared to the commercial IrO_x as well as the HEO counterpart. The superior performance is attributed to the synergistic effect and high-entropy nature of the HEPi, as well as the high quality of materials owing to the synthetic process. This study establishes a new synthesis paradigm of high-entropy polyanionic compounds for a range of applications in energy and catalysis.

2. Results and discussions

The detailed formation process of the HEPi particles synthesized *via* the high-temperature fly-through method is illustrated in Fig. 1a. The uniformly mixed precursor containing metal salts and TOPO as the phosphorous source were dissolved in ethanol with desired ratio to satisfy stoichiometry in the final product (Fig. 1a, (I)). The digital image of metal salts and mixed precursor solution is showcased in Fig. S2. The precursor solution was then sprayed to a continuous flow of aerosol droplets through atomization (Fig. 1a, (II)), where metal salts and TOPO were homogeneously confined in each droplet. Carried by an inert gas (*i.e.*, Ar), the aerosol droplets flied through the rapid heating zone, where the metal salts and TOPO were thermally decomposed to metal oxide and phosphorus during the initial increase of temperature ($< 350\ ^\circ C$) (Table S1 and Fig. S3), which then reacted with each other to form HEPi particles after the droplet reached at higher temperatures (*e.g.*, $900\ ^\circ C$) (Fig. 1a, (III)). Such a transformation from metal salt to HEPi can be completed within only hundreds of milliseconds depending on the flow rate. After exiting the heating zone, the HEPi particles were rapidly quenched to room temperature while the particles can be collected at the downstream with any targets or in a substrate-free manner. Compared with other conventional phosphating methods (*i.e.*, phosphating the pre-formed oxide) that typically take several hours, our *in-situ* phosphating method significantly decreases the processing time from hours to milliseconds through the high-temperature fly-through method (Fig. 1b). Note that conventional synthetic methods for phosphate materials are also limited to two metallic elements (Fig. 1c). In stark contrast, our high-temperature fly-through method features broad elemental choices, high elemental numbers, and excellent uniformity owing to the fast heating and quenching processes.

We synthesized a series of phosphates from unary, ternary to quinary compositions to demonstrate the broad elemental choices. Cobalt phosphate (CoPi) was synthesized as a model unary (*i.e.*, mono-metallic) phosphate material for the proof-of-concept demonstration. We first prepared a homogeneous ethanol solution containing cobalt nitrate hexahydrate (0.05 M) and TOPO (0.01 M) as precursors. The aerosol droplets (~1 μm in diameter) atomized from the above solution were carried by Ar into the tube furnace which was set at ~900 °C. The cobalt nitrate was decomposed into cobalt oxide while TOPO was decomposed to phosphorus, followed by *in-situ* phosphating reaction with each other to form CoPi. The as-prepared CoPi particles were rapidly quenched with a cooling rate of 10^5 K s^{-1} [35] and collected on a polytetrafluoroethylene (PTFE) film at the downstream (Fig. S4). The scanning transmission electron microscopy (STEM) image and the associated energy-dispersive x-ray spectroscopy (EDS) mapping reveal the homogeneous distribution of cobalt, phosphorus, and oxygen in a typical spherical particle without elemental segregation (Fig. 2a). In addition, the scanning electron microscopy (SEM) image of CoPi (Fig. S5) showcases the large quantity of hollow particles that are relatively uniform in size. In a similar process, a ternary metal phosphate (*i.e.*, MnMoWPi) was synthesized by using manganese nitrate, molybdenum nitrate, and tungsten chloride as metallic precursors (Table S1). STEM and EDS mapping results confirm the uniform elemental distribution of Mn, Mo, W, P and O within each particle (Fig. 2b). The HEPi quinary particles containing Co, Fe, Ni, Mn and Mo were prepared in the same fashion, whose SEM image showcases similar morphology as the unary particles (Fig. S6). STEM and EDS mapping results demonstrate highly uniform distribution of all five metallic elements as well as P in one HEPi particle at both high (Fig. 2c) and low magnifications (Fig. 2d).

The key parameters for preparing HEPi materials are heating temperature and cooling rate. For the heating temperature, it is important to

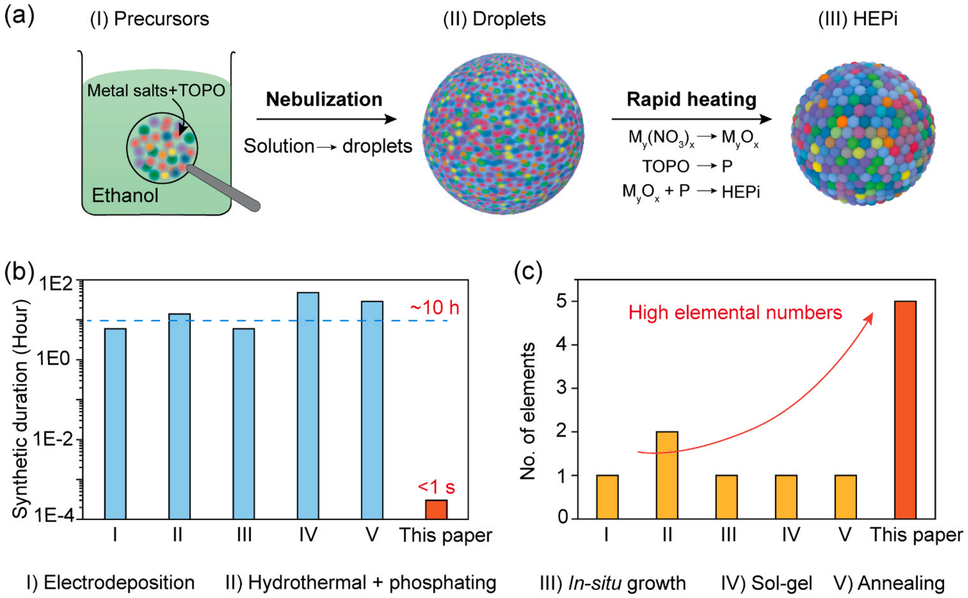

Fig. 1. Illustration of the high-temperature fly-through method. (a) Schematic illustration of the HEPi particles formation process. (I) Metal salts and TOPO dissolved in ethanol to form mixed precursors solution. (II) An aerosol droplet containing metal salts and TOPO in ethanol formed through the atomization process. (III) The HEPi particle produced by rapid heating. Comparisons between the conventional methods and our high-temperature fly-through method to prepare phosphates including (b) synthetic duration, and (c) number of elements. *Note*: I: electrodeposition [27], II: hydrothermal + phosphating method [31], III: *in-situ* growth [32], IV: Sol-gel method [33], V: Annealing [34].

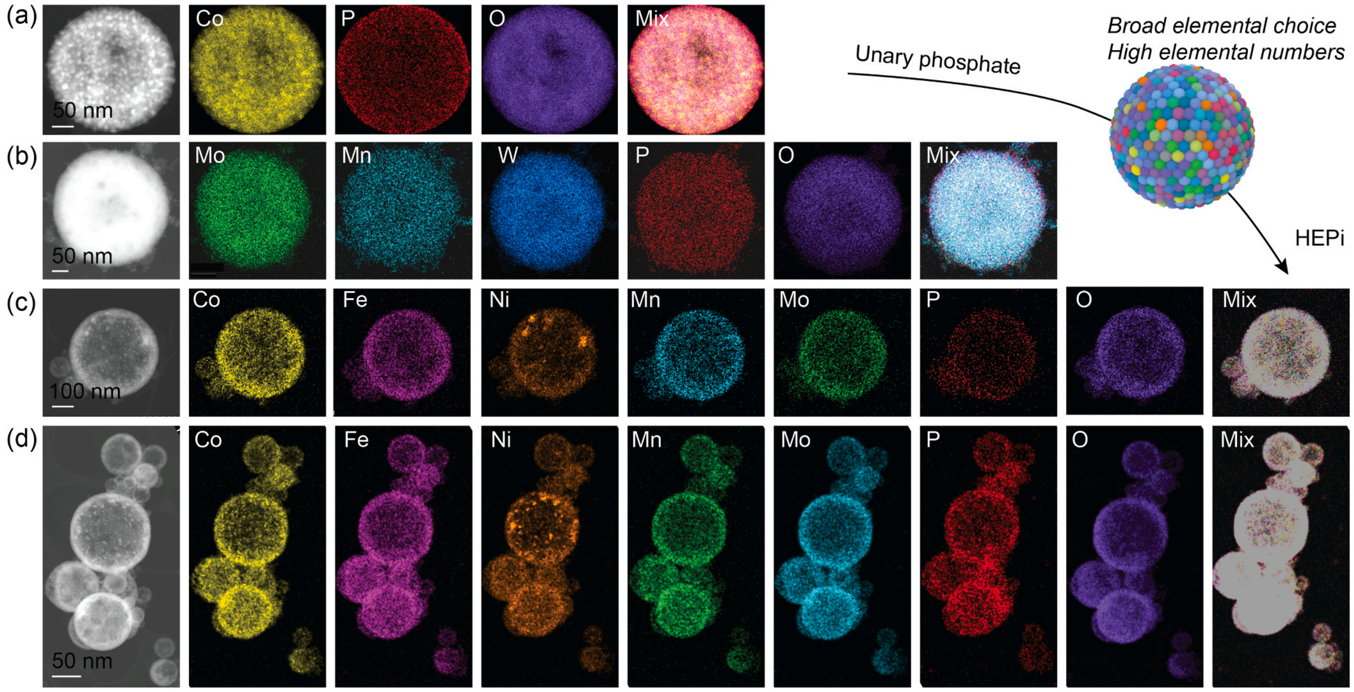

Fig. 2. Characterizations of phosphates synthesized using the high-temperature fly-through method. STEM images and the corresponding EDS mapping of phosphates (a) CoPi, (b) MnMoWPi, and (c-d) CoFeNiMnMoPi HEPi.

achieve high temperature to (1) fully decompose the precursors, especially in short heating time (less than 1 s), and (2) avoid the evaporation of P to destroy the phosphate structure. We have found that synthesizing HEPi particles at lower temperature (*e.g.*, 750 °C, incomplete decomposition, shown in Fig. S7a) or higher temperature (*e.g.*, 1000 °C, rapidly evaporation of P, shown in Fig. S7b) will lead to the production of particles in irregular shapes [36]. Synthesizing at 900 °C is optimal that can ensure a complete decomposition and stable phosphate structure. It has also been reported in previous publications that rapid quenching is essential to fabricate high-entropy materials, otherwise there will be elemental segregation or phase separation [6,37].

In addition to the homogeneous elemental distribution, the morphology of particles also plays an important role for the catalytic applications [38–42]. The decomposition of TOPO produces (1) phosphorous source, which would participate in the oxide-to-phosphate transformation, and (2) gaseous products, which would puff droplets into hollow structure. This formed hollow structure would improve mass transfer rate and decrease catalyst mass loading compared to the solid catalysts [43], boosting the normalized catalytic activity. In addition, we make a statistical count on the particle size distribution with different precursor concentrations to demonstrate the effective control over particle size by our method. Fig. S8a shows that phosphates particles prepared at different concentrations exhibit similar pattern of lognormal size distribution and the mean size of HEPi particles varies from 109 nm, 157 nm, to 200 nm, respectively, for the metal salts precursor concentrations of 0.025 M, 0.05 M, and 0.1 M. Fig. S8b shows that the particles prepared using the larger nozzle exhibit a larger mean particle size, indicating effective particle size control.

To confirm the structure of HEPi, we performed X-ray photoelectron spectroscopy (XPS) to analyze the elemental composition and the oxidation states of various elements (Fig. 3a). The spectrum of Co exhibits the peak with binding energy at 782.18 eV, which is attributed to the mixed state of 2+ and 3+, consistent with previous literatures [44,45]. In the spectrum of Fe, the peaks with binding energy of 712.08 and 725.3 eV can be assigned to Fe $2p_{3/2}$ and Fe $2p_{1/2}$ respectively, the oxidation of which also shows a mixture of 2+ and 3+ [46–48]. Moreover, Ni presents two main peaks at 852.88 and 870.8 eV, likely suggesting a 2+ oxidation state [49,50]. Mn displays two peaks at 642.08 and 654.28 eV, indicating a mixture of 2+ and 4+ [51,52]. Mo exhibits two peaks at 231.08 and 227.88 eV, which is in line with an oxidation state of 4+ [53,54]. Importantly, the spectrum of phosphorous shows the peak with binding energy at 133.0 eV, while that of O 1s shows a peak at 530.8 eV (Fig. S9). These peak positions were in good agreement with the previous reports of the phosphate group (PO_4^{3-}) [44,55].

Raman spectroscopy was then performed to validate the composition of HEPi. To exclude the influences of potential impurities, we characterized the HEO (intermediate for the HEPi formation, $FeCoNiMnMoO_x$) and TOPO (phosphorous precursor) as control samples. Fig. 3b shows that the Raman spectrum of HEPi did not contain the characteristic peaks of TOPO, indicating that the TOPO precursor was fully decomposed upon synthesis. By comparing the spectrum of HEPi with those of HEO and TOPO, a new peak at around 930 cm^{-1} was detected, which corresponds to the phosphate group [56]. In addition, Fourier-transform infrared spectroscopy (FT-IR) was employed to further differentiate HEPi from HEO (Fig. 3c). The characteristic band at around 1500 cm^{-1} can only be observed with HEO, which is attributed to metal-oxide stretching (*e.g.* Fe–O or Ni–O). In comparison, the exclusive band at around 1000 cm^{-1} can be attributed to the PO_4^{3-} group of HEPi [57]. Taken together, these characterizations confirm the successful synthesis of HEPi by our high-temperature fly-through method.

The detailed X-ray powder diffraction (XRD) characterization on HEPi particles is presented in Fig. S10. The broad peak in the range of 2 theta at 20–37° (marked as a yellow area) matched well with that of $Co_3(PO_4)_2$, $Fe_3(PO_4)_2$, $Ni_3(PO_4)_2$, and $Mn_3(PO_4)_2$. To better illustrate the crystal structure of HEPi materials, we conducted high-resolution TEM (HRTEM) with fast Fourier transform (FFT) analysis and performed detailed selected area electron diffraction (SAED). The SAED pattern (Fig. S11b) of the HEPi particles and FFT analysis of the region of interest in HRTEM (Fig. S11c) indicate the existence of metal oxides in a typical rock salt structure. The radial intensity line profile as a function of reciprocal lattice distance extracted from the SAED pattern is presented in Fig. S12. Considering that CoO, FeO, NiO, and MnO have the same crystal structure and similar lattice constants (Table S2), we only

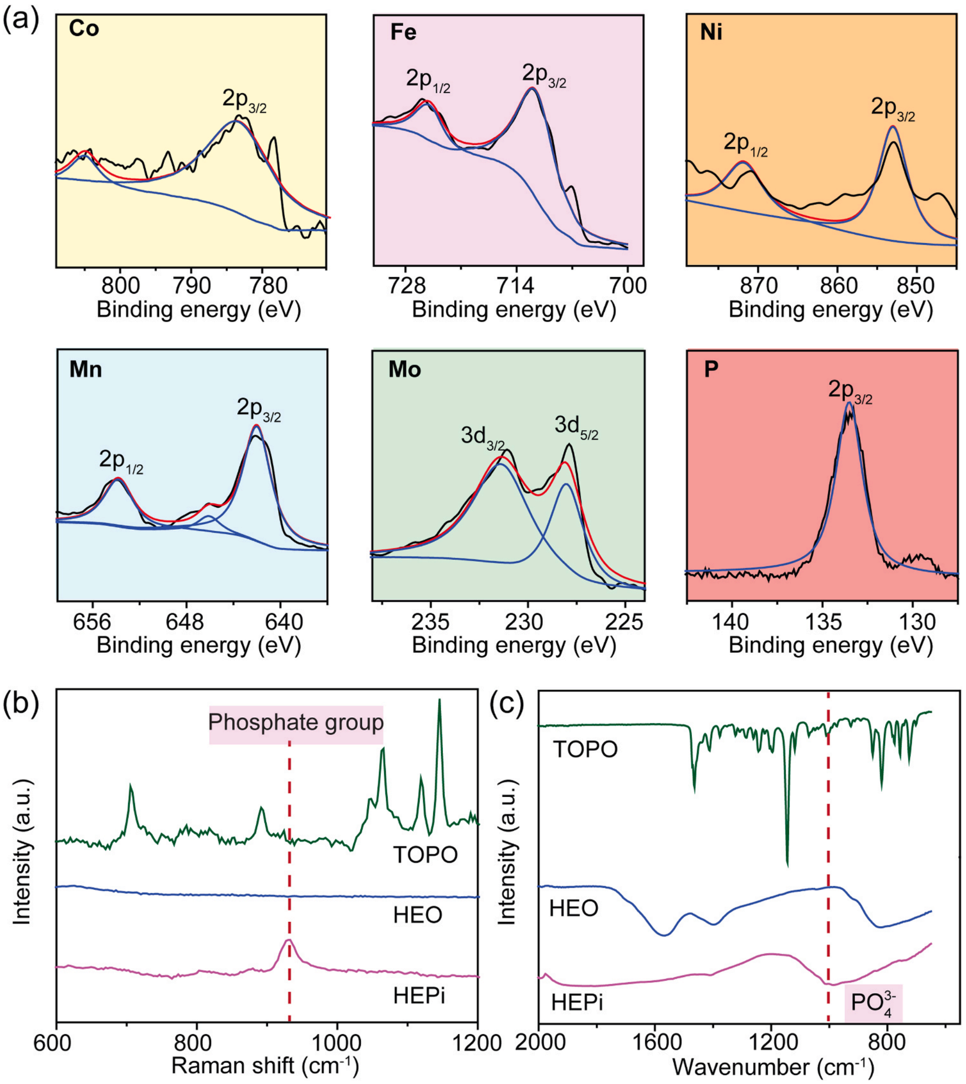

Fig. 3. Characterizations of CoFeNiMnMoPi HEPi. (a) The XPS spectra of each element collected from HEPi particles, including Co 2p, Fe 2p, Ni 2p, Mn 2p, Mo 3d and P 2p, demonstrating that the metals are in the oxidation state and P is in the valence of + 5. The comparison of (b) Raman spectra and (c) FT-IR spectra of CoFeNiMnMoPi HEPi, HEO, and TOPO samples.

list CoO as an exemplary oxide. The main peaks (marked with the red star, orange star and blue star) can be attributed to the mixture peaks of previous reported $Co_3(PO_4)_2$, $Fe_3(PO_4)_2$, $Ni_3(PO_4)_2$, and $Mn_3(PO_4)_2$. It is also noted that there is a minor amount of oxides as proved by a weak peak (marked as a black peak) in the radial intensity profile of SAED. The above results confirm the existence of high-entropy phosphates in a major phase. A bit of nuance differences observed in peak positions could be attributed to the nature of high-entropy comprising multi-principal elements with different atomic radius (elemental information is provided in Table S2). The electron energy-loss spectroscopy (EELS) analysis was also performed on the HEPi particles (Fig. S13). The distinct L-edges in the EELS profile confirm the existence of transition metal elements of Mn, Fe, Co, and Ni in the HEPi particles and their valence states are consistent with the XPS results shown in Fig. 3a.

When used as electrocatalyst, the composition of HEPi is expected to benefit the catalytic activity through synergistic effect and high-entropy stabilization. We demonstrate the utility of HEPi in OER as a proof-of-concept, which is an important reaction in the electrolysis of H_2O, CO_2 reduction, rechargeable metal-air batteries and so on [58]. The HEO synthesized by our method and a benchmark IrO_x catalyst for OER were used as control samples. In the polarization curve obtained from linear sweep voltammetry (LSV, Fig. 4a), the HEPi catalyst exhibited superior OER activity compared to the IrO_x and HEO. The overpotential of HEPi was measured to be 270 mV at 10 mA cm^{-2}, which was much smaller than those of HEO (350 mV), IrO_x (340 mV) and carbon substrate (410 mV). The effect of particle size on the overpotential is provided in Fig. S14, demonstrating HEPi particles with larger size has a slightly higher overpotential than HEPi particles with smaller size (overpotential at 10 mA cm^{-2}: 277.5 mV for HEPi with a mean particle size of 305 nm *vs.* 270 mV for HEPi with a mean particle size of 157 nm). This can be explained by that particles with smaller size have a larger surface to volume ratio, resulting in more active catalytic sites. The Tafel slope of HEPi (74 mV dec^{-1}) was also smaller than those of HEO (118 mV dec^{-1}) and IrO_x (90 mV dec^{-1}) (Fig. 4b), indicating faster OER kinetics. The comparison on the Tafel slope and overpotential between our HEPi catalyst and literature reports featuring mono- or bi- metallic phosphates are summarized in Fig. 4c [34,59–63], where the HEPi catalyst demonstrates one of the best overall performances. We also compared the LSV curves before and after 500 continuous CV cycles with a scanning rate of 50 mV s^{-1} to illustrate the catalyst stability (Fig. S15). The two traces (1st and after 500 CV scans) were by and large comparable, indicating good stability of the HEPi catalyst during OER (Fig. 4d). The electrochemical impedance spectroscopy (EIS) of the HEPi before and after 500 CV scans were presented in Fig. S16. It shows minimal

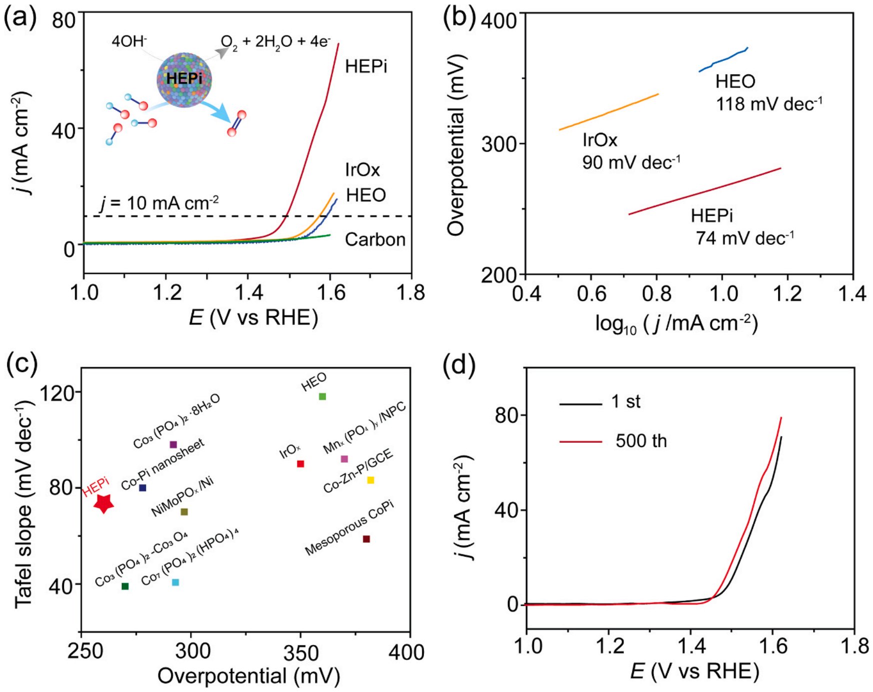

Fig. 4. OER catalytic performance of HEPi (CoFeNiMnMoPi). (a) Comparisons of polarization curves in OER performance between IrO_x, HEO and carbon substrates. (b) The corresponding Tafel slopes of different electrodes. (c) The comparison of the overpotential *vs.* Tafel slop with previous literature materials. Co-Pi nanosheet [60], $Co_3(PO_4)_2$-Co_3O_4 [61], $Co_3(PO_4)_2{\bullet}8H_2O$ [62], $Mn_x(PO_4)_y$/NPC [34], Co-Zn-P/GCE [63], mesoporous CoPi [59]. (d) The LSV curves with a scanning rate of 1 mV s^{-1} before and after 500 continuous CV cycles with a scanning rate of 50 mV s^{-1}.

resistance increase after 500 CV scans, indicating the good stability of our HEPi material. The chronoamperometric (time *vs.* current density, CA) and chronopotentiometry (time *vs.* overpotential, CP) measurements were provided in Fig. S17. The results demonstrate relatively good stability for 1 h OER operation. The catalytic performance ban be further improved by adjusting elemental ratio, [64] elemental type, [14] and morphology [65] *etc.* We envision that the application of our HEPi catalyst is not limited to OER but can be readily expanded to a range of reaction schemes with high activity and good stability.

3. Materials and methods

3.1. Materials

All the precursors were purchased from Sigma Aldrich, including: iron(III) chloride ($FeCl_3{\bullet}6H_2O$, $\geq 98\%$), cobalt(II) nitrate ($Co(NO_3)_2{\bullet}6H_2O$ $\geq 98\%$), nickel(II) nitrate hexahydrate ($Ni(NO_3)_2{\bullet}6H_2O \geq 98.5\%$), manganese(II) nitrate hydrate ($Mn(NO_3)_2{\bullet}6H_2O$, 98%), molybdenum(V) chloride ($MoCl_5$, 95%), tungsten (VI) chloride (WCl_6, $\geq 99.99\%$), tri-n-octylphosphine oxide (TOPO, 99%), Nafion solution (5 wt.%) and carbon black (ETJENBALCK EC-600JD).

3.2. Preparation of phosphate particles

All phosphates were synthesized through desired metal salts precursors (0.05 M) at equivalent ratios and TOPO (0.01 M) dissolved in ethanol. Then, the mixed precursors were atomized into small droplets by a collision nebulizer (CH Technologies (USA), Inc.) under the pressure of ~20 psi using argon as the carrier gas. Then the droplets flowed through a diffusion dryer filled with silicone gel, where most of the solvent was absorbed, forming solid precursor particles. Further carried into the tube furnace (~900 °C), these solid precursor particles decomposed to the metal oxide, phosphorous and other gases (*e.g.*, water and CO_x). The phosphorous would *in-situ* phosphate the metal oxide into metal phosphates and the other gases would puff the particles into a hollow structure [36,66]. Then the rapid quenching (with a cooling rate of 10^5 K s^{-1}) [35] solidifies this hollow HEPi particles into one phase. The final product was collected on a Millipore membrane with a pore size of 0.65 μm.

3.3. Preparation of HEO particles

Like the fabrication procedure of phosphates, the HEO particles were synthesized through desired metal salts precursors (0.05 M) at equivalent ratios dissolved in ethanol without addition of TOPO. The following procedure is same with the steps operated in the preparation process of phosphates.

3.4. Characterization

SEM was conducted on a Hitachi SU-70 field emission microscope at 10 kV for morphological characterizations. STEM imaging along with EELS analysis and EDS elemental mapping were performed on Hitachi SU9000 STEM. TEM/HRTEM imaging with SAED was performed on Hitachi H9500 TEM. The Raman testing was performed with Horiba Jobin Yvon Raman Microscope, with a laser source of 532 nm. FT-IR spectra was performed on a Thermo Nicolet Nexus 6700 spectrometer over the rage of 400–4000 cm^{-1}. The XPS spectra were taken on a high sensitivity Kratos AXIS spectrometer to probe the valence state of the elements on the surface. The absorbance spectra of carbon black were measured on a Lambda UV–vis spectrometer from 300 to 2100 nm with an integrating sphere (PerkinElmer, USA). X-ray diffraction (XRD) was performed using a D8 Advanced (Bruker AXS, WI, USA) with a scan rate of 5° min^{-1}.

3.5. Electrochemical measurements

We chose the OER as a model reaction to illustrate the catalytic performance. The electrochemical measurements were performed on a three-electrode system in 1 M KOH electrolyte at room temperature in ambient environment. The glassy carbon electrode deposited with catalyst serves as work electrode, a graphite rod as counter electrode and Ag/AgCl as reference electrode. The preparation of working electrode is modified according to the previous reports [67,68]. Catalyst powders (2 mg), carbon powders (1.5 mg) was dispersed in 1 ml of 3:1 v/v water/isopropanol mixed solvent with Nafion solution (80 μl), then the mixture was ultrasonicated for at least 40 min to generate a homogeneous ink. The glassy carbon electrode first polished using 0.05 mm alumina powder and cleaned using DI water before electrochemical measurements. The catalyst ink (∼4 μl) was dropped on a glassy carbon electrode with a diameter of 3 mm, giving a catalyst loading ∼0.07 mg cm^{-2}, and dried at room temperature first and at an oven at the temperature of 60 °C for at least 2 h before electrochemical test. For comparisons, HEO, IrO$_x$ and bare glassy carbon electrode also prepared as work electrode under same parameters for electrochemical test.

The LSV was measured from − 0.1 to 0.7 V (*vs.* reference electrode) with a scanning rate of 10 mV s^{-1}. The cycling stability of the synthesis HEPi particles was determined by cyclic voltammetry at 50 mV s^{-1} for 500 cycles. All the potentials were converted and referred to the reversible hydrogen potential (RHE) according to the equation $E_{vs\ RHE} = E_{vs\ Ag/AgCl} + E^0_{Ag/AgCl\ vs\ RHE} + 0.059^{*}pH$. The electrochemical impedance spectroscopy (EIS) test was carried out on the working electrodes and the spectra were collected in a frequency range of 1–100 K Hz with an amplitude of 10.0 mV. The chronoamperometric (time v*s.* current density, CA) measurement was carried out using an overpotential of 270 mV and the chronopotentiometry (time *vs.* overpotential, CP) measurement was carried out using a current density of 10 mA cm^{-2}.

4. Conclusion

In conclusion, we for the first time report the synthesis of HEPi catalysts through a high-temperature fly-through method. The successful phosphating of up to five metallic elements was enabled by: (1) Confining metal salts and TOPO uniformly within one droplet, (2) Rapid high-temperature oxide-to-phosphate transformation; and (3) Fast quenching to avoid elemental and phase separation. By this method, we successfully synthesized a series of phosphates, from mono metallic, trimetallic to high-entropy phosphate species. The elemental distribution was found to be highly uniform by STEM-EDS mapping, and the characteristic phosphate structure can be verified by XPS, Raman, and FT-IR. As a proof-of-concept, we demonstrate the utility of our HEPi catalyst in OER, where superior catalytic activity (270 mV of overpotential at 10 mA cm$^{-2)}$ was measured, much smaller than that of the HEO counterpart (350 mV) and the benchmark IrO$_x$ catalyst (340 mV). The HEPi catalyst can be applied to other reactions beyond OER; meanwhile the facile, efficient, and scalable synthesis method can open a new avenue for the discovery of a range of polyanionic materials for energy and catalysis applications.

CRediT authorship contribution statement

L. Hu, H. Qiao, X. Wang and Q Dong designed the experiments. H. Qiao, X. Wang, G. Chen and C. Yang carried out the synthesis of materials. H. Qiao, Q Dong and M. Wu carried out the OER experiments. H. Zheng and K. He performed analytical TEM characterization. L. Hu, H. Qiao, X. Wang and Q. Dong collectively wrote the paper. All authors commented on the final manuscript.

Declaration of Competing Interest

The authors declare that they have no known competing financial interests or personal relationships that could have appeared to influence the work reported in this paper.

Acknowledgements

We acknowledge the support of the Maryland Nanocenter, its Surface Analysis Center and AIM Lab. K.H. and H.Z. acknowledge the support of Clemson University Startup Fund and the use of Clemson Electron Microscopy Facility.

Appendix A. Supporting information

Supplementary data associated with this article can be found in the online version at doi:10.1016/j.nanoen.2021.106029.

References

[1] N.T.-C. Nguyen, P. Asghari-Rad, P. Sathiyamoorthi, A. Zargaran, C.S. Lee, H.S. Kim, Ultrahigh high-strain-rate superplasticity in a nanostructured high-entropy alloy, Nat. Commun. 11 (2020) 2736, https://doi.org/10.1038/s41467-020-16601-1.

[2] Y. Gogotsi, Transition metal carbides go 2D, Nat. Mater. 14 (2015) 1079–1080, https://doi.org/10.1038/nmat4386.

[3] E.P. George, D. Raabe, R.O. Ritchie, High-entropy alloys, Nat. Rev. Mater. 4 (2019) 515–534, https://doi.org/10.1038/s41578-019-0121-4.

[4] O. Mashtalir, M. Naguib, V.N. Mochalin, Y. Dall'Agnese, M. Heon, M.W. Barsoum, Y. Gogotsi, Intercalation and delamination of layered carbides and carbonitrides, Nat. Commun. 4 (2013) 1716, https://doi.org/10.1038/ncomms2664.

[5] H. Zhang, A.W. Maijenburg, X. Li, S.L. Schweizer, R.B. Wehrspohn, Bifunctional heterostructured transition metal phosphides for efficient electrochemical water splitting, Adv. Funct. Mater. 30 (2020), 2003261, https://doi.org/10.1002/adfm.202003261.

[6] Y. Yao, Z. Huang, P. Xie, S.D. Lacey, R.J. Jacob, H. Xie, F. Chen, A. Nie, T. Pu, M. Rehwoldt, D. Yu, M.R. Zachariah, C. Wang, R. Shahbazian-Yassar, J. Li, L. Hu, Carbothermal shock synthesis of high-entropy-alloy nanoparticles, Science 359 (2018) 1489–1494, https://doi.org/10.1126/science.aan5412.

[7] Y. Yao, Z. Liu, P. Xie, Z. Huang, T. Li, D. Morris, Z. Finfrock, J. Zhou, M. Jiao, J. Gao, Y. Mao, J. (John) Miao, P. Zhang, R. Shahbazian-Yassar, C. Wang, G. Wang, L. Hu, Computationally aided, entropy-driven synthesis of highly efficient and durable multi-elemental alloy catalysts, Sci. Adv. 6 (2020), eaaz0510, https://doi.org/10.1126/sciadv.aaz0510.

[8] P. Shi, W. Ren, T. Zheng, Z. Ren, X. Hou, J. Peng, P. Hu, Y. Gao, Y. Zhong, P. K. Liaw, Enhanced strength–ductility synergy in ultrafine-grained eutectic high-entropy alloys by inheriting microstructural lamellae, Nat. Commun. 10 (2019) 489, https://doi.org/10.1038/s41467-019-08460-2.

[9] F. Zhang, Y. Wu, H. Lou, Z. Zeng, V.B. Prakapenka, E. Greenberg, Y. Ren, J. Yan, J. S. Okasinski, X. Liu, Y. Liu, Q. Zeng, Z. Lu, Polymorphism in a high-entropy alloy, Nat. Commun. 8 (2017) 15687, https://doi.org/10.1038/ncomms15687.

[10] M.W. Glasscott, A.D. Pendergast, S. Goines, A.R. Bishop, A.T. Hoang, C. Renault, J. E. Dick, Electrosynthesis of high-entropy metallic glass nanoparticles for designer, multi-functional electrocatalysis, Nat. Commun. 10 (2019) 2650, https://doi.org/10.1038/s41467-019-10303-z.

[11] T.A.A. Batchelor, J.K. Pedersen, S.H. Winther, I.E. Castelli, K.W. Jacobsen, J. Rossmeisl, High-entropy alloys as a discovery platform for electrocatalysis, Joule 3 (2019) 834–845, https://doi.org/10.1016/j.joule.2018.12.015.

[12] P. Buchwalter, J. Rosé, P. Braunstein, Multimetallic catalysis based on heterometallic complexes and clusters, Chem. Rev. 115 (2015) 28–126, https://doi.org/10.1021/cr500208k.

[13] X. Bo, R.K. Hocking, S. Zhou, Y. Li, X. Chen, J. Zhuang, Y. Du, C. Zhao, Capturing the active sites of multimetallic (oxy)hydroxides for the oxygen evolution reaction, Energy Environ. Sci. 13 (2020) 4225–4237, https://doi.org/10.1039/D0EE01609H (10.1039.D0EE01609H).

[14] A. Sarkar, L. Velasco, D. Wang, Q. Wang, G. Talasila, L. de Biasi, C. Kübel, T. Brezesinski, S.S. Bhattacharya, H. Hahn, B. Breitung, High entropy oxides for reversible energy storage, Nat. Commun. 9 (2018) 3400, https://doi.org/10.1038/s41467-018-05774-5.

[15] C.M. Rost, E. Sachet, T. Borman, A. Moballegh, E.C. Dickey, D. Hou, J.L. Jones, S. Curtarolo, J.-P. Maria, Entropy-stabilized oxides, Nat. Commun. 6 (2015) 8485, https://doi.org/10.1038/ncomms9485.

[16] P. Sarker, T. Harrington, C. Toher, C. Oses, M. Samiee, J.-P. Maria, D.W. Brenner, K.S. Vecchio, S. Curtarolo, High-entropy high-hardness metal carbides discovered by entropy descriptors, Nat. Commun. 9 (2018) 4980, https://doi.org/10.1038/s41467-018-07160-7.

[17] M. Cui, C. Yang, B. Li, Q. Dong, M. Wu, S. Hwang, H. Xie, X. Wang, G. Wang, L. Hu, High-Entropy Metal Sulfide Nanoparticles Promise High-Performance Oxygen Evolution Reaction, Adv. Energy Mater. 11 (2021), 2002887, https://doi.org/10.1002/aenm.202002887.

[18] C.R. McCormick, R.E. Schaak, Simultaneous Multication Exchange Pathway to High-Entropy Metal Sulfide Nanoparticles, J. Am. Chem. Soc. 143 (2021) 1017–1023, https://doi.org/10.1021/jacs.0c11384.

[19] Z. Gong, Y. Yang, Recent advances in the research of polyanion-type cathode materials for Li-ion batteries, Energy Environ. Sci. 4 (2011) 3223, https://doi.org/10.1039/c0ee00713g.

[20] C. Masquelier, L. Croguennec, Polyanionic (phosphates, silicates, sulfates) frameworks as electrode materials for rechargeable Li (or Na) batteries, Chem. Rev. 113 (2013) 6552–6591, https://doi.org/10.1021/cr3001862.

[21] P. Barpanda, L. Lander, S. Nishimura, A. Yamada, Polyanionic insertion materials for sodium-ion batteries, Adv. Energy Mater. 8 (2018), 1703055, https://doi.org/10.1002/aenm.201703055.

[22] G. Chen, Q. Huang, T. Wu, L. Lu, Polyanion sodium vanadium phosphate for next generation of sodium-ion batteries—a review, Adv. Funct. Mater. 30 (2020), 2001289, https://doi.org/10.1002/adfm.202001289.

[23] N.F. Dummer, J.K. Bartley, G.J. Hutchings, Chapter 4 - vanadium phosphate materials as selective oxidation catalysts, in: B.C. Gates, H. Knözinger (Eds.), Adv.

Catal., Academic Press, 2011, pp. 189–247, https://doi.org/10.1016/B978-0-12-387772-7.00004-6.

[24] S. Treviño, A. Díaz, E. Sánchez-Lara, B.L. Sanchez-Gaytan, J.M. Perez-Aguilar, E. González-Vergara, Vanadium in biological action: chemical, pharmacological aspects, and metabolic implications in diabetes mellitus, Biol. Trace Elem. Res. 188 (2019) 68–98, https://doi.org/10.1007/s12011-018-1540-6.

[25] D. Ballesteros-Plata, A. Infantes-Molina, E. Rodríguez-Aguado, P. Braos-García, J. Jiménez-Jiménez, E. Rodríguez-Castellón, Zirconium phosphate heterostructures as catalyst support in hydrodeoxygenation reactions, Catalysts 7 (2017) 176, https://doi.org/10.3390/catal7060176.

[26] M.W. Kanan, Y. Surendranath, D.G. Nocera, Cobalt–phosphate oxygen-evolving compound, Chem. Soc. Rev. 38 (2009) 109–114, https://doi.org/10.1039/B802885K.

[27] M.W. Kanan, D.G. Nocera, In situ formation of an oxygen-evolving catalyst in neutral water containing phosphate and Co^{2+}, Science 321 (2008) 1072–1075, https://doi.org/10.1126/science.1162018.

[28] M.W. Kanan, J. Yano, Y. Surendranath, M. Dincă, V.K. Yachandra, D.G. Nocera, Structure and valency of a cobalt−phosphate water oxidation catalyst determined by in situ X-ray spectroscopy, J. Am. Chem. Soc. 132 (2010) 13692–13701, https://doi.org/10.1021/ja1023767.

[29] Y. Surendranath, M.W. Kanan, D.G. Nocera, Mechanistic studies of the oxygen evolution reaction by a cobalt-phosphate catalyst at neutral pH, J. Am. Chem. Soc. 132 (2010) 16501–16509, https://doi.org/10.1021/ja106102b.

[30] Z. Yi, J. Ye, N. Kikugawa, T. Kako, S. Ouyang, H. Stuart-Williams, H. Yang, J. Cao, W. Luo, Z. Li, Y. Liu, R.L. Withers, An orthophosphate semiconductor with photooxidation properties under visible-light irradiation, Nat. Mater. 9 (2010) 559–564, https://doi.org/10.1038/nmat2780.

[31] X. Zhang, J. Li, Y. Sun, Q. Liu, J. Guo, Hybridized $Ni(PO_3)_2$-$MnPO_4$ nanosheets array with excellent electrochemical performances for overall water splitting and supercapacitor, Electrochim. Acta 299 (2019) 835–843, https://doi.org/10.1016/j.electacta.2019.01.074.

[32] J. Rong, F. Qiu, T. Zhang, Y. Fang, J. Xu, Y. Zhu, Self-directed hierarchical $Cu_3(PO_4)_2$/Cu-BDC nanosheets array based on copper foam as an efficient and durable electrocatalyst for overall water splitting, Electrochim. Acta 313 (2019) 179–188, https://doi.org/10.1016/j.electacta.2019.05.030.

[33] M. Pramanik, C. Li, M. Imura, V. Malgras, Y.-M. Kang, Y. Yamauchi, Ordered mesoporous cobalt phosphate with crystallized walls toward highly active water oxidation electrocatalysts, Small 12 (2016) 1709–1715, https://doi.org/10.1002/smll.201503187.

[34] S. Wang, G. Nam, P. Li, H. Jang, J. Wang, M.G. Kim, Z. Wu, X. Liu, J. Cho, $Mn_x(PO_4)_y$ /NPC as a high performance bifunctional electrocatalyst for oxygen electrode reactions, ChemCatChem 11 (2019) 1222–1227, https://doi.org/10.1002/cctc.201801753.

[35] Y. Yang, B. Song, X. Ke, F. Xu, K.N. Bozhilov, L. Hu, R. Shahbazian-Yassar, M. R. Zachariah, Aerosol synthesis of high entropy alloy nanoparticles, Langmuir 36 (2020) 1985–1992, https://doi.org/10.1021/acs.langmuir.9b03392.

[36] X. Wang, Z. Huang, Y. Yao, H. Qiao, G. Zhong, Y. Pei, C. Zheng, D. Kline, Q. Xia, Z. Lin, J. Dai, M.R. Zachariah, B. Yang, R. Shahbazian-Yassar, L. Hu, Continuous 2000 K droplet-to-particle synthesis, Mater. Today 35 (2020) 106–114, https://doi.org/10.1016/j.mattod.2019.11.004.

[37] P.-C. Chen, X. Liu, J.L. Hedrick, Z. Xie, S. Wang, Q.-Y. Lin, M.C. Hersam, V. P. Dravid, C.A. Mirkin, Polyelemental nanoparticle libraries, Science 352 (2016) 1565–1569, https://doi.org/10.1126/science.aaf8402.

[38] S.-S. Xu, X.-W. Lv, Y.-M. Zhao, T.-Z. Ren, Z.-Y. Yuan, Engineering morphologies of cobalt oxide/phosphate-carbon nanohybrids for high-efficiency electrochemical water oxidation and reduction, J. Energy Chem. 52 (2021) 139–146, https://doi.org/10.1016/j.jechem.2020.04.054.

[39] S. Akbar, A. Anwar, M.Z. Noon, J.M. Elliott, A.M. Squires, Platinum as an electrocatalyst: effect of morphological aspects of Pt/Pt-based materials, Mater. Sci. Technol. 35 (2019) 1–11, https://doi.org/10.1080/02670836.2018.1495878.

[40] K. Yamamoto, T. Imaoka, W.-J. Chun, O. Enoki, H. Katoh, M. Takenaga, A. Sonoi, Size-specific catalytic activity of platinum clusters enhances oxygen reduction reactions, Nat. Chem. 1 (2009) 397–402, https://doi.org/10.1038/nchem.288.

[41] M. Che, C.O. Bennett, The influence of particle size on the catalytic properties of supported metals, in: D.D. Eley, H. Pines, P.B. Weisz (Eds.), Adv. Catal., Academic Press, 1989, pp. 55–172, https://doi.org/10.1016/S0360-0564(08)60017-6.

[42] Y. Sun, L. Zhuang, J. Lu, X. Hong, P. Liu, Collapse in crystalline structure and decline in catalytic activity of pt nanoparticles on reducing particle size to 1 nm, J. Am. Chem. Soc. 129 (2007) 15465–15467, https://doi.org/10.1021/ja076177b.

[43] G. Prieto, H. Tüysüz, N. Duyckaerts, J. Knossalla, G.-H. Wang, F. Schüth, Hollow nano- and microstructures as catalysts, Chem. Rev. 116 (2016) 14056–14119, https://doi.org/10.1021/acs.chemrev.6b00374.

[44] L. Xie, R. Zhang, L. Cui, D. Liu, S. Hao, Y. Ma, G. Du, A.M. Asiri, X. Sun, High-performance electrolytic oxygen evolution in neutral media catalyzed by a cobalt phosphate nanoarray, Angew. Chem. Int. Ed. 56 (2017) 1064–1068, https://doi.org/10.1002/anie.201610776.

[45] T. Zhou, Y. Du, S. Yin, X. Tian, H. Yang, X. Wang, B. Liu, H. Zheng, S. Qiao, R. Xu, Nitrogen-doped cobalt phosphate@nanocarbon hybrids for efficient electrocatalytic oxygen reduction, Energy Environ. Sci. 9 (2016) 2563–2570, https://doi.org/10.1039/C6EE01297C.

[46] J. Yu, T. Zhang, Y. Sun, X. Li, X. Li, B. Wu, D. Men, Y. Li, Hollow FeP/Fe_3O_4 Hybrid nanoparticles on carbon nanotubes as efficient electrocatalysts for the oxygen evolution reaction, ACS Appl. Mater. Interfaces 12 (2020) 12783–12792, https://doi.org/10.1021/acsami.9b21927.

[47] L. Gan, J. Fang, M. Wang, L. Hu, K. Zhang, Y. Lai, J. Li, Preparation of double-shell Co_9S_8/Fe_3O_4 embedded in S/N co-decorated hollow carbon nanoellipsoid derived from Bi-Metal organic frameworks for oxygen evolution reaction, J. Power Sour. 391 (2018) 59–66, https://doi.org/10.1016/j.jpowsour.2018.04.082.

[48] M. Wu, M. Cui, L. Wu, S. Hwang, C. Yang, Q. Xia, G. Zhong, H. Qiao, W. Gan, X. Wang, D. Kline, M.R. Zachariah, D. Su, T. Li, L. Hu, Hierarchical polyelemental nanoparticles as bifunctional catalysts for oxygen evolution and reduction reactions, Adv. Energy Mater. 10 (2020), 2001119, https://doi.org/10.1002/aenm.202001119.

[49] Z. Zhou, L. Wei, Y. Wang, H.E. Karahan, Z. Chen, Y. Lei, X. Chen, S. Zhai, X. Liao, Y. Chen, Hydrogen evolution reaction activity of nickel phosphide is highly sensitive to electrolyte pH, J. Mater. Chem. A 5 (2017) 20390–20397, https://doi.org/10.1039/C7TA06000A.

[50] A. Han, H. Chen, Z. Sun, J. Xu, P. Du, High catalytic activity for water oxidation based on nanostructured nickel phosphide precursors, Chem. Commun. 51 (2015) 11626–11629, https://doi.org/10.1039/C5CC02626A.

[51] M.-Q. Wang, C. Ye, S.-J. Bao, M.-W. Xu, Controlled synthesis of $Mn_3(PO_4)_2$ hollow spheres as biomimetic enzymes for selective detection of superoxide anions released by living cells, Microchim. Acta 184 (2017) 1177–1184, https://doi.org/10.1007/s00604-017-2112-8.

[52] K. Jin, J. Park, J. Lee, K.D. Yang, G.K. Pradhan, U. Sim, D. Jeong, H.L. Jang, S. Park, D. Kim, N.-E. Sung, S.H. Kim, S. Han, K.T. Nam, Hydrated manganese(II) phosphate ($Mn_3 (PO_4)_2 \cdot 3H_2 O$) as a water oxidation catalyst, J. Am. Chem. Soc. 136 (2014) 7435–7443, https://doi.org/10.1021/ja5026529.

[53] D. Dinda, Md.E. Ahmed, S. Mandal, B. Mondal, S.K. Saha, Amorphous molybdenum sulfide quantum dots: an efficient hydrogen evolution electrocatalyst in neutral medium, J. Mater. Chem. A 4 (2016) 15486–15493, https://doi.org/10.1039/C6TA06101J.

[54] L.-N. Zhang, S.-H. Li, H.-Q. Tan, S.U. Khan, Y.-Y. Ma, H.-Y. Zang, Y.-H. Wang, Y.-G. Li, MoP/Mo_2C@C: a new combination of electrocatalysts for highly efficient hydrogen evolution over the entire pH range, ACS Appl. Mater. Interfaces 9 (2017) 16270–16279, https://doi.org/10.1021/acsami.7b03823.

[55] S.K. Pilli, T.E. Furtak, L.D. Brown, T.G. Deutsch, J.A. Turner, A.M. Herring, Cobalt-phosphate (Co-Pi) catalyst modified Mo-doped BiVO4 photoelectrodes for solar water oxidation, Energy Environ. Sci. 4 (2011) 5028, https://doi.org/10.1039/c1ee02444b.

[56] M.D. Fontana, K. Ben Mabrouk, T.H. Kauffmann, Raman spectroscopic sensors for inorganic salts, in: J. Yarwood, R. Douthwaite, S. Duckett (Eds.), Spectrosc. Prop. Inorg. Organomet. Compd., Royal Society of Chemistry, Cambridge, 2013, pp. 40–67, https://doi.org/10.1039/9781849737791-00040.

[57] E.J. Elzinga, D.L. Sparks, Phosphate adsorption onto hematite: an in situ ATR-FTIR investigation of the effects of pH and loading level on the mode of phosphate surface complexation, J. Colloid Interface Sci. 308 (2007) 53–70, https://doi.org/10.1016/j.jcis.2006.12.061.

[58] M. Tahir, L. Pan, F. Idrees, X. Zhang, L. Wang, J.-J. Zou, Z.L. Wang, Electrocatalytic oxygen evolution reaction for energy conversion and storage: a comprehensive review, Nano Energy 37 (2017) 136–157, https://doi.org/10.1016/j.nanoen.2017.05.022.

[59] M.S. Al-Sharif, P. Arunachalam, T. Abiti, M.S. Amer, M. Al-Shalwi, M.A. Ghanem, Mesoporous cobalt phosphate electrocatalyst prepared using liquid crystal template for methanol oxidation reaction in alkaline solution, Arab. J. Chem. 13 (2020) 2873–2882, https://doi.org/10.1016/j.arabjc.2018.07.017.

[60] Z.-S. Cai, Y. Shi, S.-S. Bao, Y. Shen, X.-H. Xia, L.-M. Zheng, Bioinspired engineering of cobalt-phosphonate nanosheets for robust hydrogen evolution reaction, ACS Catal. 8 (2018) 3895–3902, https://doi.org/10.1021/acscatal.7b04276.

[61] B. Jin, Y. Li, J. Wang, F. Meng, S. Cao, B. He, S. Jia, Y. Wang, Z. Li, X. Liu, Promoting oxygen evolution reaction of Co-based catalysts (Co_3O_4, CoS, CoP, and CoN) through photothermal effect, Small 15 (2019), 1903847, https://doi.org/10.1002/smll.201903847.

[62] J. Qi, Y.-P. Lin, D. Chen, T. Zhou, W. Zhang, R. Cao, Autologous cobalt phosphates with modulated coordination sites for electrocatalytic water oxidation, Angew. Chem. Int. Ed. 59 (2020) 8917–8921, https://doi.org/10.1002/ange.202001737.

[63] L. Qian, Y. Miao, Nanosheet organized flower-like Co/Zn phosphate on nickel foam for efficient water splitting in both acid and basic solutions, Polyhedron 160 (2019) 213–218, https://doi.org/10.1016/j.poly.2018.12.050.

[64] T. Li, Y. Yao, Z. Huang, P. Xie, Z. Liu, M. Yang, J. Gao, K. Zeng, A.H. Brozena, G. Pastel, M. Jiao, Q. Dong, J. Dai, S. Li, H. Zong, M. Chi, J. Luo, Y. Mo, G. Wang, C. Wang, R. Shahbazian-Yassar, L. Hu, Denary oxide nanoparticles as highly stable catalysts for methane combustion, Nat. Catal. 4 (2021) 62–70, https://doi.org/10.1038/s41929-020-00554-1.

[65] X. Wang, Q. Dong, H. Qiao, Z. Huang, M.T. Saray, G. Zhong, Z. Lin, M. Cui, A. Brozena, M. Hong, Q. Xia, J. Gao, G. Chen, R. Shahbazian-Yassar, D. Wang, L. Hu, Continuous synthesis of hollow high-entropy nanoparticles for energy and catalysis applications, Adv. Mater. 32 (2020), 2002853, https://doi.org/10.1002/adma.202002853.

[66] B. Ren, M. Fan, Q. Liu, J. Wang, D. Song, X. Bai, Hollow NiO nanofibers modified by citric acid and the performances as supercapacitor electrode, Electrochim. Acta 92 (2013) 197–204, https://doi.org/10.1016/j.electacta.2013.01.009.

[67] Y.-F. Xu, M.-R. Gao, Y.-R. Zheng, J. Jiang, S.-H. Yu, Nickel/Nickel(II) oxide nanoparticles anchored onto cobalt(IV) diselenide nanobelts for the electrochemical production of hydrogen, Angew. Chem. Int. Ed. 52 (2013) 8546–8550, https://doi.org/10.1002/anie.201303495.

[68] Z. Jin, J. Lv, H. Jia, W. Liu, H. Li, Z. Chen, X. Lin, G. Xie, X. Liu, S. Sun, H. Qiu, Nanoporous Al-Ni-Co-Ir-Mo high-entropy alloy for record-high water splitting activity in acidic environments, Small 15 (2019), 1904180, https://doi.org/10.1002/smll.201904180.